Pd Nanoparticles Decorated by Oxidized Ru Clusters for Efficient C–H/C–H Coupling of Arenes

Shingo Hasegawa,[1] Shunta Tokutake,[1] Koji Harano,[2,3] Ken Motokura*[1]

[1]Department of Chemistry and Life Science, Yokohama National University, 79-5 Tokiwadai, Hodogaya-ku, Yokohama 240-8501, Japan.

[2]Center for Basic Research on Materials, National Institute for Materials Science, 1-1 Namiki, Tsukuba, Ibaraki 305-0044, Japan.

[3]Research Center for Autonomous Systems Materialogy (ASMat), Institute of Integrated Research, Institute of Science Tokyo, 4259 Nagatsuda-cho, Midori-ku, Yokohama, Kanagawa 226–8501, Japan

KEYWORDS: Bimetallic catalyst, Palladium, Ruthenium, C–H bond activation, oxidative coupling, arene, biaryl

ABSTRACT: Oxidative homocoupling of arenes is a challenging but attractive method converting non-activated aromatics into biaryl compounds. Applications and mechanistic understanding of bimetallic nanocatalysts for arene C–H bond activation are limited at present. In this study, we found that Pd-Ru bimetallic catalyst supported on Al_2O_3 showed remarkably high catalytic activity for the oxidative homocoupling of arenes owing to the synergistic effect between Pd and Ru. Structural analyses by high-angle annular dark-field scanning transmission electron microscopy with energy dispersive X-ray spectroscopy and X-ray absorption spectroscopy revealed that Pd nanoparticles were decorated by partially oxidized Ru clusters. Mechanistic studies indicated that the arene C–H bond cleavage was the rate-determining step and proceeded by concerted metalation deprotonation mechanism. It was proposed that the role of Ru is promoting the C–H activation step by generating electron deficient Pd sites, which was supported by DFT calculations. The Ru-decorated Pd nanoparticles showed large turnover numbers for simple arenes.

Introduction. The biaryl structure is an essential structural unit included by many important chemicals such as bioactive compounds and pharmaceuticals.[1,2] Oxidative homocoupling of arenes via direct C(aryl)–H bond activation is a highly efficient molecular transformation affording biaryls in one step (**Figure 1a**).[3–6] In particular, when using molecular oxygen as an oxidant, only H_2O was generated as a by-product. The high atom/step economy is the clear advantage of the oxidative coupling over the conventional coupling reactions requiring halogenated aromatics.[7,8] Metal nanoparticle (NP) catalysts for the arene homocoupling reactions have been developed by using Pd, Au, or Ru as an active metal element with metal oxides, organic polymers, or carbon as a support (**Figure 1b**).[9–15] Zhou and Wang reported that Pd clusters with average size of 1.2 nm supported on hypercrosslinked polymer functionalized by dicarboxylic acid (Pd/HCP) showed large turnover numbers (TONs) for the oxidative homocoupling of benzene using O_2 in the presence of trifluoromethanesulfonic acid and acetic acid.[13] According to the report by Serna and Corma, Au NPs (~3 nm) on TiO_2 catalyzed the homocoupling reactions of benzene derivatives with O_2 under acid free conditions.[11] Co_3O_4- and ZrO_2-supported Au NPs (Au/Co_3O_4 and Au/ZrO_2) were developed by Ishida and Tokunaga for the regioselective homocoupling of di-substituted benzenes such as dimethyl phthalate under O_2 in acetic acid solvent.[12] Feuillastre and Pieters demonstrated that carbon-supported Ru NPs (Ru/C) catalyzed the homocoupling of 2-arylpyridines with high regioselectivity to less sterically hindered products using $FeCl_3$ as an oxidant in toluene solvent.[15]

It has been demonstrated that the synergistic effects of different metal elements are of great importance for developing highly active, selective, and durable heterogeneous catalysts for various reactions.[16–34] Some reports described the effectiveness of bimetallic catalysts for arene C–H bond activation reactions;[35–39] for instance, we have recently developed the carbon-supported Rh-Ru bimetallic oxide cluster catalyst ($RhRuO_x$/C) that showed remarkably high catalytic activity for cross-dehydrogenative coupling of arenes and carboxylic acid under O_2 due to the synergy of Rh and Ru.[39] Jiang demonstrated that carbon supported Cu-Ag NPs (CuAg/C) showed improved catalytic activity and selectivity for benzene hydroxylation by H_2O_2 compared to monometallic counterparts.[35] Zhang reported the enhanced catalytic activity of CuPd alloy NPs supported on reduced graphene oxide (CuPd/rGO) for the C–H acylation of 2-phenylpyridine by benzyl alcohol using *tert*-butyl peroxybenzoate as an oxidant.[38] On the other hand, bimetallic catalysts have not been applied to the oxidative homocoupling of arenes to the best of our knowledge. Thus, it is essential research target to develop highly active bimetallic catalyst for arene homocoupling and elucidate the origin of synergistic catalysis.

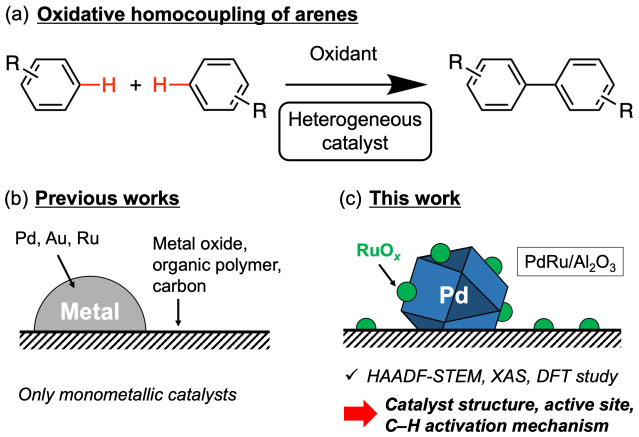

Figure 1. (a) Oxidative homocoupling of arenes. (b) Previously reported heterogeneous catalysts for the oxidative homocoupling of arenes. (c) Al_2O_3-supported Pd NPs decorated by partially oxidized Ru clusters ($PdRu/Al_2O_3$) developed for the arene homocoupling (this work).

In this study, we developed Al_2O_3-supported Pd NPs decorated by partially oxidized Ru clusters (RuO_x) for the oxidative homocoupling of arenes (**Figure 1c**). Remarkable synergy of Pd and Ru was observed; the turnover number of Pd for benzene homocoupling was enhanced ~4 times by Ru. Electron microscopic and spectroscopic methods clarified the formation of Pd nanoparticles (NPs) decorated by partially oxidized Ru clusters. Mechanistic experiments indicated that C–H bond activation step was rate-determining and proceeded by concerted metalation deprotonation mechanism. It was proposed that electron deficient Pd sites generated by Ru act as active sites for C–H activation. DFT calculated free energy profile of benzene C–H bond activation by model clusters supported the proposed mechanism. $PdRu/Al_2O_3$ was applicable to simple arenes and high TONs were achieved without strong acids such as trifluoromethanesulfonic acid.

Results and Discussion. Alumina-supported monometallic catalysts, M/Al_2O_3 (M = Pd, Pt, Ir, Rh, Ru), were initially tested for the oxidative homocoupling of benzene (**Figures 2a, 2b**). The supported metal catalysts were prepared by the deposition of preformed metal NPs, which were synthesized by the reduction of precursor metal ions by ethylene glycol in the presence of polyvinylpyrrolidone. The catalytic tests were carried out with 1 mL of benzene and 1 mL of acetic acid at 150 °C under 0.6 MPa of O_2 for 16 h. Pd/Al_2O_3 showed the highest yield of biphenyl (373 μmol), whereas the catalytic activities of the other monometallic catalysts for the oxidative homocoupling were much lower. Pt and Ir catalysts afforded low biphenyl yield (<30 μmol) and no biphenyl was detected after the reaction with Rh or Ru catalysts. In addition to the oxidative homocoupling, the oxidative acetoxylation of benzene also proceeded to form phenyl acetate (**3a**). The selectivity of Pd/Al_2O_3 to homocoupling over acetoxylation was high (97%).

Pd-based bimetallic catalysts, PdM/Al_2O_3 (M = Ru, Ir, Pt, Rh), were prepared by the co-reduction of equimolar mixture of precursors and applied to the oxidative homocoupling of benzene (**Figure 2b**). $PdRu/Al_2O_3$ exhibited remarkably enhanced catalytic activity for oxidative homocoupling compared to monometallic Pd catalyst, although the pure Ru catalyst was inactive for the homocoupling. Biphenyl yield increased from 373 μmol to 728 μmol by the synergy of Pd and Ru, whereas the selectivity was almost retained (96% and 97% for PdRu and Pd, respectively). In contrast to the PdRu catalyst, the other bimetallic catalysts showed lower biphenyl yield than that by the pure Pd catalyst. The effect of the ratio between Pd and Ru was further studied; biphenyl yield and turnover number (TON) based on Pd were plotted against the Ru content (x) in **Figure 2c**. TON reached the maximum value of 146 at Pd-Ru ratio of ~1:1, which was almost four times that of pure Pd catalyst (37). On the other hand, Pd-rich bimetallic catalysts (x: 0.1–0.5) showed similar biphenyl yields. For the equimolar PdRu NPs, different supports were tested (**Table S1**). The observed catalytic activity was in the order of $PdRu/Al_2O_3$ > $PdRu/TiO_2$ > PdRu/hydrotalcite > PdRu/MgO. Hereafter, we will discuss $PdRu/Al_2O_3$ with equimolar composition as an optimized catalyst.

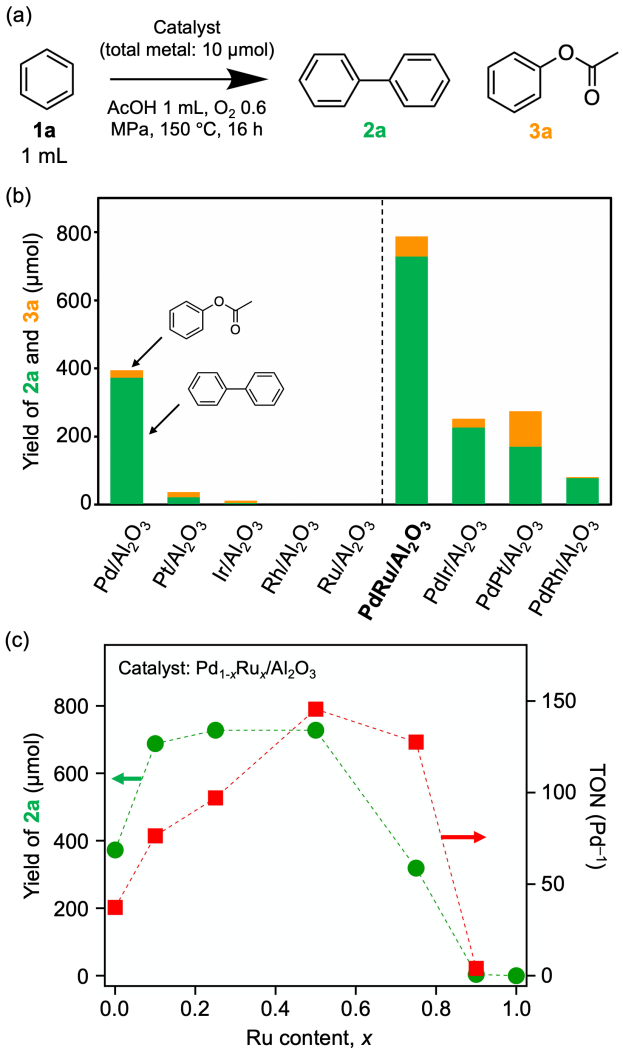

Figure 2. (a) Oxidative homocoupling of benzene. (b) Yield of **2a** (green) and **3a** (orange) in μmol unit for monometallic and bimetallic catalysts with the total metal amount of 10 μmol. (c) The product yields in μmol unit as a function of Ru content in $Pd_{1-x}Ru_x/Al_2O_3$ catalyst.

The structure of PdRu/Al_2O_3 was analyzed by high-angle annular dark-field scanning transmission electron microscopy (HAADF-STEM) with energy dispersive X-ray spectroscopy (EDS). **Figure 3a** shows the representative HAADF image of PdRu/Al_2O_3. In the left region of **Figure 3a**, particles with diameters of ~16 nm were observed, whereas ~2 nm sized particles were distributed in the entire region. EDS elemental mapping revealed that the larger particles were Pd NPs (size: 16 ± 2 nm, **Figures 3d, S1a**) and smaller ones correspond to Ru clusters (size: 2.3 ± 0.4 nm, **Figures 3e, S1b**). Although Ru clusters were distributed on both Pd NPs and Al_2O_3 support, all the observed Pd NPs were decorated by Ru clusters (**Figure 3f**). Thus, the active site of PdRu/Al_2O_3 catalyst was the surface of Pd NPs modified by Ru clusters.

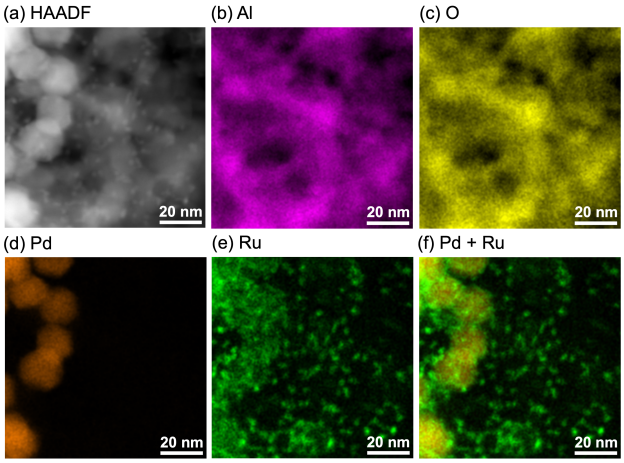

Figure 3. (a) HAADF-STEM image and (b) Al, (c) O, (d) Pd, (e) Ru, and (f) Pd + Ru elemental maps of PdRu/Al_2O_3 obtained by STEM-EDS.

The structure of Ru-decorated Pd NPs was further studied by high-resolution HAADF-STEM. Representative HAADF images of NPs **#1**–**#3** are displayed in **Figures 4a**, **S2a**, and **S3a**, respectively. All of the three NPs showed clear lattice planes with interplanar spacing of 0.23 nm (**Figures 4b**, **S2b**, **S3b**), which is assignable to {111} planes of Pd.[40,41] The hexagonal particle images and direction of {111} planes suggested that the Pd NPs have cuboctahedral three-dimensional structures (**Figures 4c**, **S2c**, **S3c**). Since most of observed Pd NPs showed nearly hexagonal images, the fundamental structure of Pd core in PdRu/Al_2O_3 was thought to be cuboctahedron, which is a well-known morphology of Pd NPs.[42,43] The distribution of Ru on single Pd NP was not uniform but localized to several spots with dimension of a few nm (**Figures 4e**, **S2e, S3e**). Thus, the formation of Ru-decorated Pd NPs rather than Pd@Ru core-shell NPs was supported.

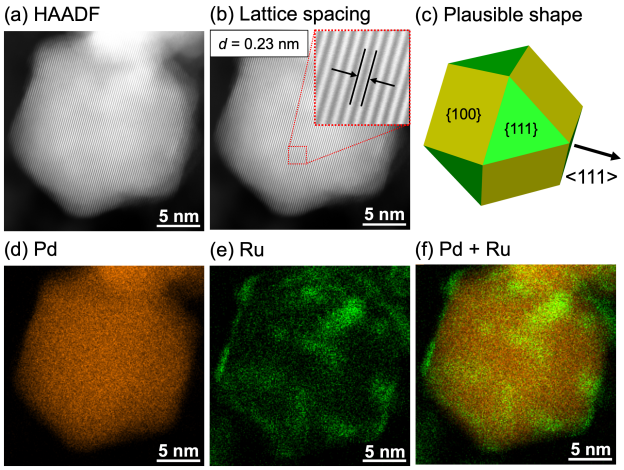

Figure 4. Structural analysis of NP **#1** in PdRu/Al_2O_3 by high-resolution STEM imaging: (a) HAADF-STEM image, (b) enlarged image showing lattice spacing, (c) plausible three-dimensional structure of Pd core, and (d–f) elemental maps obtained by STEM-EDS for (d) Pd, (e) Ru, and (f) Pd + Ru.

The electronic states and coordination structures of Pd and Ru were studied by X-ray absorption fine structure (XAFS) analysis. **Figures 5a** and **5b** display the Pd K- and Ru K-edge X-ray absorption near edge structures (XANES) of PdRu/Al_2O_3 with those of standard samples. The XANES spectra indicated that Pd in the catalyst was in metallic state, whereas Ru was partially oxidized. Consistent results were obtained in the analysis of extended X-ray absorption fine structures (EXAFS). Pd K-edge EXAFS of PdRu/Al_2O_3 was well reproduced by the fitting with the Pd–Pd bond (**Figure 4c**, **Table 1**). The Pd–Pd coordination number (CN) was calculated to be 8.9 ± 1.2, indicating the formation of Pd NPs. The spectral feature of Ru K-edge FT-EXAFS of the catalyst suggested the presence of the Ru–O bond (**Figure 4d**). The curve-fitting analysis resulted in the CNs of 5.2 ± 0.7 for Ru–Ru bond and 1.8 ± 0.7 for Ru–O bond, supporting the partial oxidation of Ru clusters. The smaller Ru–Ru CN than that of Pd–Pd was in agreement with the results of electron microscopic analysis. Collectively, HAADF-STEM, EDS, and XAFS analyses revealed the formation of cuboctahedral Pd NPs (16 nm) decorated by partially oxidized Ru clusters (2.3 nm).

According to the characterization results of monometallic Pd/Al_2O_3 by TEM and XAFS analysis (**Figure S4**), the Pd NPs contained in the monometallic catalyst was smaller than that of Pd core of PdRu/Al_2O_3. TEM images of the Pd catalyst showed the size distribution with mean diameter of 4.6 nm and standard deviation of 0.7 nm. Considering the smaller surface-to-volume ratio of the PdRu catalyst, the catalytic activity of surface Pd atoms in PdRu system was much higher than that in monometallic Pd catalyst.

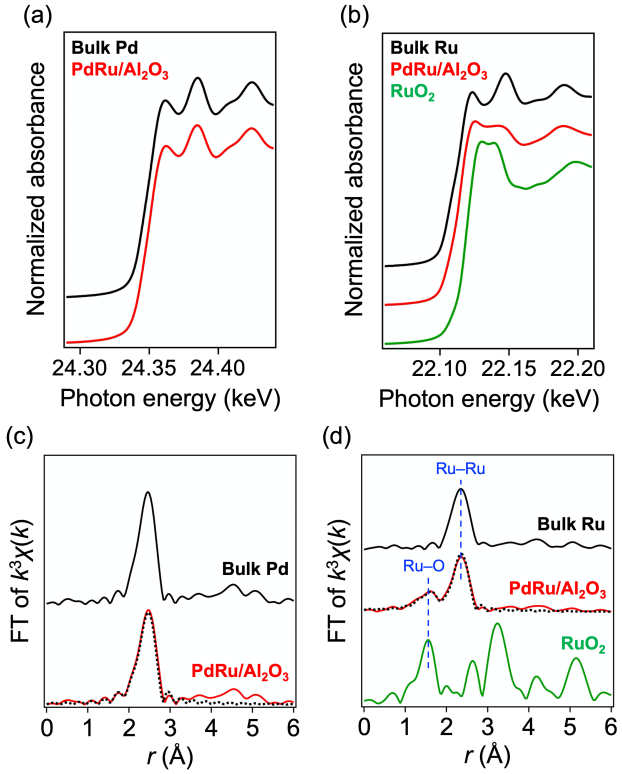

Figure 5. (a) Pd K- and (b) Ru K-edge XANES spectra. (c) Pd K- and (d) Ru K-edge FT-EXAFS spectra with fitting data (dashed curves).

Table 1. Structural Parameters of $PdRu/Al_2O_3$ Obtained by Curve-Fitting Analysis of Pd and Ru K-edge EXAFS

Edge	Bond	CN	r (Å)	σ^2 (Å^2)	R (%)
Pd K	Pd–Pd	8.9 ± 1.2	2.74 ± 0.01	0.0066 ± 0.0013	4.9
Ru K	Ru–Ru	5.2 ± 0.7	2.67 ± 0.01	0.0082 ± 0.0015	6.4
	Ru–O	1.8 ± 0.7	2.02 ± 0.03	0.0077 ± 0.0074	

XAFS analysis of $PdRu/Al_2O_3$ after the oxidative homocoupling of benzene revealed that the oxidation states of Pd and Ru did not significantly change. Pd NPs retained the metallic state (**Figure S5a**), although further oxidation of Ru NPs slightly proceeded (**Figure S5b**).

To obtain insight into the reaction mechanism, kinetic isotope effect (KIE) was evaluated for $PdRu/Al_2O_3$ and Pd/Al_2O_3 by comparing the reaction rate for benzene and benzene-d_6 (**Figure 6a**). Both bimetallic and monometallic catalysts showed clear KIE (PdRu: 3.3, Pd: 5.0), indicating that the cleavage of aryl C–H bond was rate-determining step. According to the results of control experiments illustrated in **Figure 6b**, acetic acid was indispensable for the oxidative homocoupling. **Figure 6c** summarizes the TONs of $PdRu/Al_2O_3$ for the reactions with mono-substituted benzenes. There was a trend that electron withdrawing groups increased the reactivity, although the unsubstituted benzene showed much higher TON (453) under the same conditions probably due to the steric effect. The primary KIE, pivotal role of acetic acid, and substituent effect indicated that the C–H bond activation proceeded by concerted metalation deprotonation (CMD) mechanism (**Figure 7**, step (ii)).[44–48] The lower KIE of the PdRu catalyst than that of the Pd catalyst suggested the promotion of C–H bond activation step by Ru. Arrhenius plot of PdRu- and Pd-catalyzed oxidative homocoupling of benzene revealed that the apparent activation energy for Pd/Al_2O_3 (114 kJ/mol) was decreased by Ru to 73 kJ/mol (**Figure 6d**). Considering the catalyst structure clarified by HAADF-STEM, EDS, and XAFS analyses, it was proposed that the electron deficient Pd sites generated by the surface modification by partially oxidized Ru clusters worked as the active site for C–H bond activation with decreased activation barrier (**Figure 7**). The presence of electron deficient Pd in $PdRu/Al_2O_3$ was supported by the results of X-ray photoelectron spectroscopy (XPS) in **Figure S7**. The plausible catalytic cycle was illustrated in **Figure 7**:[46,48] surface oxidation by O_2 in the presence of AcOH generates Pd–OAc site (step (i)); the C–H bond of arene is activated by CMD mechanism (step (ii)); the second arene is activated similarly (step (iii)); reductive elimination produces biaryls and recovers the catalyst (step (iv)). The surface oxidation of Pd by O_2 in acetic acid (step (i)) was confirmed by XPS (**Figure S8**).

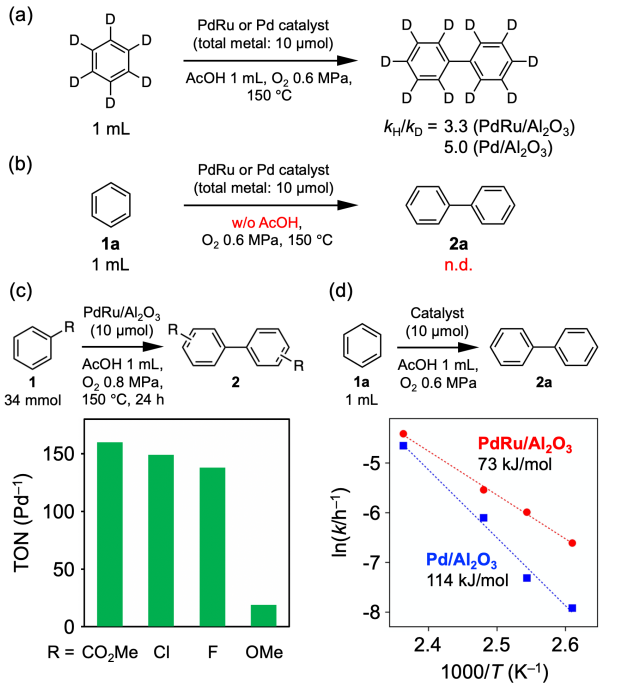

Figure 6. (a) Kinetic isotope effect and (b) Arrhenius plot of the oxidative homocoupling of benzene catalyzed by $PdRu/Al_2O_3$ and Pd/Al_2O_3.

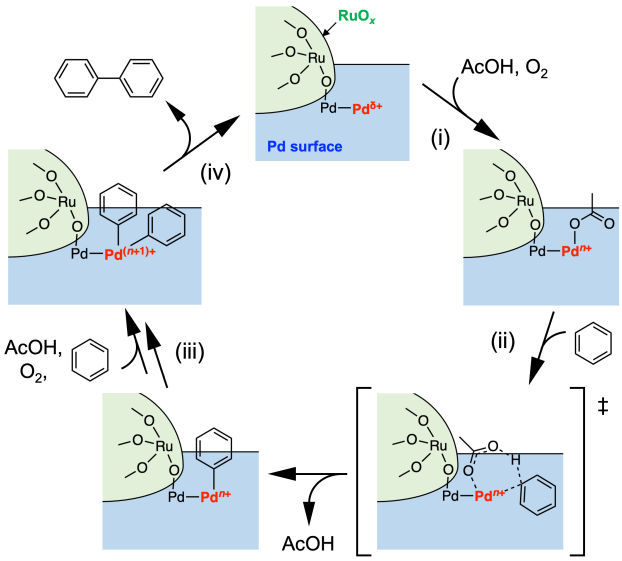

Figure 7. Proposed reaction mechanism.

The proposed C–H bond activation mechanism (**Figure 7**, step (ii)) was supported by theoretical calculations based on density functional theory (DFT). DFT calculations were carried out by Gaussian 16 program[49]. PBE functional[50] and basis sets of LANL2DZ (Pd, Ru), 6-31G(d,p) (C, H), and 6-31+G(d) (O) were applied for optimization and frequency calculations. Electronic energies were obtained by single point calculations using PBE-D3 functional[50,51] and basis sets of cc-pVTZ-PP (Pd, Ru), cc-pVTZ (C, H), and aug-cc-pVTZ (O). Solvent effects on the electronic energies were included by polarizable continuum model (PCM) with parameters for benzene. The structures of Pd clusters have been studied by DFT calculations with PBE functional.[52,53] We employed the most stable isomer of Pd_{10} with pseudo-C_{3v} symmetry recently reported by Da Silva as a model of pure Pd catalyst (**Figure S6a**).[53] The model of bimetallic catalyst was constructed by attaching oxidized Ru(IV) to the surface of the Pd_{10} cluster (**Figure S6b**). Gibbs energies of the structural isomers of the bimetallic model were compared (**Figure S7**) and the most energetically favorable one (isomer **#1**) was applied in this study. The surface decoration of Pd_{10} core by oxidized Ru did not induce significant change of the core structure. The Pd_{10} core in the bimetallic system was positively charged and the net charge was calculated to be 0.817 by natural bond orbital (NBO) analysis (**Figure S11a**).

Gibbs free energies of C–H activation for different initial structures were systematically calculated for monometallic and bimetallic systems (**Table S4**, **Figures S12–S23**). **Figure 8** illustrates the most energetically favorable pathways in both systems. The bimetallic model showed a lower activation Gibbs energy (133 kJ/mol) than that of monometallic system (148 kJ/mol), which is qualitatively consistent with experimental results. The Pd cluster core in **A-TS1** was more positively charged than that in **B-TS1** (**Figure S11**), whereas the geometric structures of the transition states were similar. Therefore, the decrease of activation barrier was ascribed to the electron deficient state of the Pd core induced by oxidized Ru. Thus, DFT calculations supported the proposal that electron deficient Pd site acts as the active site for C–H bond activation on $PdRu/Al_2O_3$. The transition state structures were further analyzed by More O'Ferrall-Jencks plot (**Figure S15a**).[39,54–56] Since **A-TS1** and **B-TS1** were located at the CMD region (**Figure S15b**), CMD mechanism was supported by theoretical results as well as experimental observations.

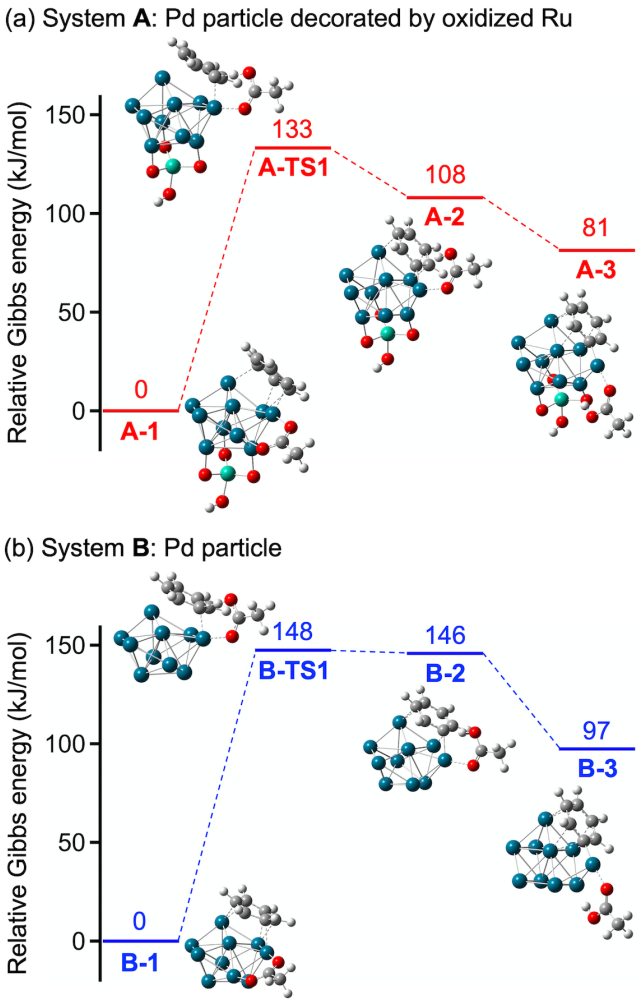

Figure 8. Free energy profiles of the benzene C–H bond activation by (a) $Pd_{10}Ru_1O_3(OH)_1$ and (b) Pd_{10} model clusters.

The applicability of $PdRu/Al_2O_3$ catalyst to simple arenes (**1a–1g**) was tested and summarized in **Table 2**. Pd-based TON of $PdRu/Al_2O_3$ for benzene reached 453 with the reaction conditions described in **Table 2**. TONs of reported metal NP catalysts for arene homocoupling are described in **Table S6**. It was confirmed that oxidative homocoupling of mono-substituted (**1b–1e**) and di-substituted (**1f**) benzenes proceeded with the PdRu catalyst and that high (>100) TON was achieved for some substrates (**1b–1d**). The trend of reactivity suggested that both electronic and steric effects of substituents have large impact. When using diphenyl ether (**1g**) as a substrate, intramolecular C–H/C–H coupling to dibenzofurane proceeded with very high TON (>1000).

Table 2. Substrate scope[a]

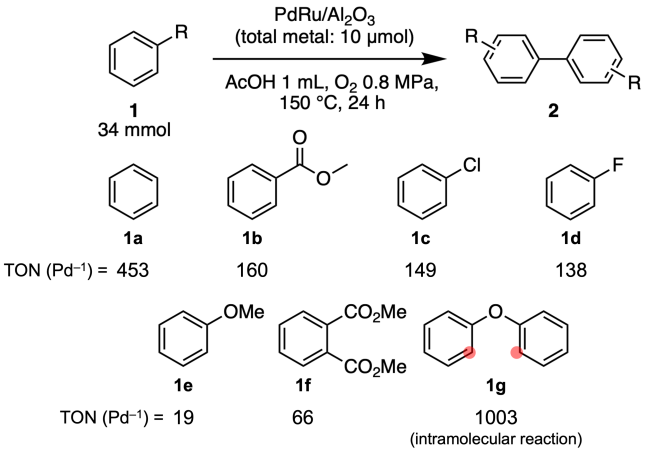

[a]Conditions: metal (10 μmol), arene (34 mmol), acetic acid (1 mL), O_2 (0.8 MPa), 150 °C, 24 h. Product selectivity of substituted benzenes was summarized in **Table S4**.

Conclusions. In summary, we developed Al_2O_3-supported Pd-Ru bimetallic catalyst by simple co-reduction method. The $PdRu/Al_2O_3$ catalyst showed high TONs for the oxidative homocoupling of simple arenes, due to the synergy between Pd and Ru. HAADF-STEM, EDS, and XAFS analyses revealed that the surface of cuboctahedral Pd NPs (16 nm) was decorated by partially oxidized Ru clusters (2.3 nm). KIE and the effects of acetic acid and substituents indicated that C(aryl)–H bond cleavage was the rate-determining step of $PdRu/Al_2O_3$-catalyzed oxidative homocoupling and proceeded by CMD mechanism. Arrhenius plot revealed the decrease of apparent activation energy by Ru from 114 kJ/mol (Pd/Al_2O_3) to 73 kJ/mol ($PdRu/Al_2O_3$). It was proposed that the surface modification by partially oxidized Ru clusters generates electron deficient Pd sites working as the active site for C–H bond activation. DFT calculations on model systems supported the proposed mechanism.

Materials and Methods. Detailed description of used materials, experimental methods, and theoretical calculations was included in the Supporting Information.

AUTHOR INFORMATION

Corresponding Author

Ken Motokura – *Department of Chemistry and Life Science, Yokohama National University, Yokohama 240-8501, Japan*
E-mail: motokura-ken-xw@ynu.ac.jp

Authors

Shingo Hasegawa – *Department of Chemistry and Life Science, Yokohama National University, Yokohama 240-8501, Japan*
Shunta Tokutake – *Department of Chemistry and Life Science, Yokohama National University, Yokohama 240-8501, Japan*

Koji Harano – *Center for Basic Research on Materials, National Institute for Material Science, Ibaraki 305–0044, Japan; Research Center for Autonomous Systems Materialogy (ASMat), Institute of Integrated Research, Institute of Science Tokyo, 4259 Nagatsuda-cho, Midori-ku, Yokohama, Kanagawa 226–8501, Japan*

Notes

The authors declare no competing financial interest.

ASSOCIATED CONTENT

Supporting Information

The Supporting Information is available free of charge on the ACS Publications website.

Details of experimental and theoretical methods; additional data of catalytic tests; elemental analysis results; additional HAADF-STEM, EDS, TEM, XAFS, XPS, and DFT data; product selectivity in catalytic reactions; summary of arene homocoupling in previous reports and this study. Cartesian coordinates of optimized structures (PDF).

ACKNOWLEDGMENT

This research was financially supported by JSPS KAKENHI (Grant Nos. JP22K20554, JP23K13602, JP23H04874, JP23K23131) and Tokyo Ohka Foundation for the Promotion of Science and Technology. Calculations were partly performed at the Research Center for Computational Science, Okazaki, Japan (Project: 22-IMS-C237, 23-IMS-C283, 24-IMS-C258). XAFS measurements were conducted with the approval of the Photon Factory Advisory Committee (Proposal Nos. 2022G033, 2024G058).

REFERENCES

1. Bringmann, G.; Mortimer, A. J. P.; Keller, P. A.; Gresser, M. J.; Garner, J.; Breuning, M. Atroposelective Synthesis of Axially Chiral Biaryl Compounds. *Angew. Chem., Int. Ed.* **2005**, *44*, 5384–5427.
2. Wang, J.; Liu, C.-F.; Zheng, Q.; Rao, G.-W. C–H Functionalization of Biaryl Compounds. *Eur. J. Org. Chem.* **2020**, 3737–3765.
3. Yang, Y.; Lan, J.; You, J. Oxidative C–H/C–H Coupling Reactions between Two (Hetero)arenes. *Chem. Rev*. **2017**, *117*, 8787–8863.
4. Wang, J.; Su, P.; Abdolmohammadi, S.; Vessally, E. A Walk around the Application of Nanocatalysts for Cross-Dehydrogenative Coupling of C–H Bonds. *RSC Adv.* **2019**, *9*, 41684–41702.
5. Tian, T.; Li, Z.; Li, C.-J. Cross-Dehydrogenative Coupling: A Sustainable Reaction for C–C Bond Formations. *Green Chem.* **2021**, *23*, 6789–6862.
6. Hasegawa, S.; Motokura, K. Design Strategy of Metal Nanoparticle Catalysis for C–H Bond Activation Reactions. *ChemCatChem* **2024**, *16*, e202301531.
7. Miyaura, N.; Suzuki, A. Palladium-Catalyzed Cross-Coupling Reactions of Organoboron Compounds. *Chem. Rev.* **1995**, *95*, 2457–2483.
8. Hassan, J.; Sévignon, M.; Gozzi, C.; Schulz, E.; Lemaire, M. Aryl–Aryl Bond Formation One Century after the Discovery of the Ullmann Reaction. *Chem. Rev.* **2002**, *102*, 1359–1469.
9. Neal, L. M.; Hagelin-Weaver, H. E. C–H Activation and C–C Coupling of 4-Methylpyridine using Palladium Supported on Nanoparticle Alumina. *J. Mol. Catal. A* **2008**, *284*, 141–148.
10. Ishida, T.; Tsunoda, R.; Zhang, Z.; Hamasaki, A.; Honma, T.; Ohashi, H.; Yokoyama, T.; Tokunaga, M. Supported Palladium Hydroxide-Catalyzed Intramolecular Double C–H Bond Functionalization for Synthesis of Carbazoles and Dibenzofurans. *Appl. Catal. B* **2014**, *150*, 523–531.
11. Serna, P.; Corma, A. A Residue-Free Production of Biaryls using Supported Gold Nanoparticles. *J. Catal.* **2014**, *315*, 41–47.
12. Ishida, T.; Aikawa, S.; Mise, Y.; Akebi, R.; Hamasaki, A.; Honma, T.; Ohashi, H.; Tsuji, T.; Yamamoto, Y.; Miyasaka, M.; Yokoyama, T.; Tokunaga, M. Direct C–H Arene Homocoupling over

Gold Nanoparticles Supported on Metal Oxides. *ChemSusChem* **2015**, *8*, 695–701.
13. Liu, Y.; Zou, C.; Wang, K.; Bian, Z.; Jiang, S.; Zhou, Y.; Wang, J. Palladium Clusters on Dicarboxyl-Functional Hypercrosslinked Porous Polymers for Oxidative Homocoupling of Benzene with O_2. *Mol. Catal.* **2021**, *505*, 111487
14. Wang, K.; Cui, W.; Bian, Z.; Liu, Y.; Jiang, S.; Zhou, Y.; Wang, J. Size and Stability Modulation of Pd Nanoparticles on Porous Hypercrosslinked Ionic Polymer for Heterogeneous Aerobic Oxidative Coupling of Diaryl Ether. *Appl. Catal. B* **2021**, *281*, 119425.
15. Gao, L. Feuillastre, S.; Clavier, G.; Pieters, G. Cross-Dehydrogenative Homocoupling of 2-Aryl-N-Heterocycles and Application to the Synthesis of Phenylpyridine Borane Dimers. *Eur. J. Org. Chem.* **2022**, e202201164.
16. Liu, L.; Corma, A. Bimetallic Sites for Catalysis: From Binuclear Metal Sites to Bimetallic Nanoclusters and Nanoparticles *Chem. Rev.* **2023**, *123*, 4855–4933.
17. Nakaya, Y.; Furukawa, S. Catalysis of Alloys: Classification, Principles, and Design for a Variety of Materials and Reactions. *Chem. Rev.* **2023**, *123*, 5859–5947.
18. Ding, K.; Cullen, D. A.; Zhang, L.; Cao, Z.; Roy, A. D.; Ivanov, I. N.; Cao, D. A General Synthesis Approach for Supported Bimetallic Nanoparticles via Surface Inorganometallic Chemistry. *Science* **2018**, *362*, 560-564.
19. Nakagawa, Y.; Takada, K.; Tamura, M.; Tomishige, K. Total Hydrogenation of Furfural and 5-Hydroxymethylfurfural over Supported Pd-Ir Alloy Catalyst. *ACS Catal.* **2014**, *4*, 2718-2726.
20. Tang, M.; Mao, S.; Li, M.; Wei, Z.; Xu, F.; Li, H.; Wang, Y. RuPd Alloy Nanoparticles Supported on N-Doped Carbon as an Efficient and Stable Catalyst for Benzoic Acid Hydrogenation. *ACS Catal*. **2015**, *5*, 3100-3107.
21. Huang, B.; Kobayashi, H.; Yamamoto, T.; Matsumura, S.; Nishida, Y.; Sato, K.; Nagaoka, K.; Kawaguchi, S.; Kubota, Y.; Kitagawa, H. Solid-Solution Alloying of Immiscible Ru and Cu with Enhanced CO Oxidation Activity. *J. Am. Chem. Soc.* **2017**, *139*, 4643-4646.
22. Chen, G.; Zhao, Y.; Fu, G.; Duchesne, P. N.; Gu, L.; Zheng, Y.; Weng, X.; Chen, M.; Zhang, P.; Pao, C.-W.; Lee, J.-F.; Zheng, N. Interfacial Effects in Iron-Nickel Hydroxide–Platinum Nanoparticles Enhance Catalytic Oxidation. *Science* **2014**, *344*, 495-499.
23. Wu, C. H.; Liu, C.; Su, D.; Xin, H. L.; Fang, H.-T.; Eren, B.; Zhang, S.; Murray, C. B.; Salmeron, M. B. Bimetallic synergy in cobalt–palladium nanocatalysts for CO oxidation. *Nat. Catal*. **2019**, *2*, 78-85.
24. Huang, X.; Akdim, O.; Douthwaite, M.; Wang, K.; Zhao, L.; Lewis, R. J.; Pattisson, S.; Daniel, I. T.; Miedziak, P. J.; Shaw, G.; Morgan, D. J.; Althahban, S. M.; Davies, T. E.; He, Q.; Wang, F.; Fu, J.; Bethell, D.; McIntosh, S.; Kiely, C. J.; Hutchings, G. J. Au–Pd separation enhances bimetallic catalysis of alcohol oxidation. *Nature* **2022**, *603*, 271-275.
25. Ryoo, R.; Kim, J.; Jo, C.; Han, S. W.; Kim, J.-C.; Park, H.; Han, J.; Shin, H. S.; Shin, J. W. Rare-earth–platinum alloy nanoparticles in mesoporous zeolite for catalysis. *Nature* **2020**, *585*, 221-224.
26. Liu, L.; Lopez-Haro, M.; Lopes, C. W.; Li, C.; Concepcion, P.; Simonelli, L.; Calvino, J. J.; Corma, A. Regioselective generation and reactivity control of subnanometric platinum clusters in zeolites for high-temperature catalysis. *Nat. Mater.* **2019**, *18*, 866-873.
27. Gorey, T. J.; Zandkarimi, B.; Li, G.; Baxter, E. T.; Alexandrova, A. N.; Anderson, S. L. Coking-Resistant Sub-Nano Dehydrogenation Catalysts: PtnSnx/SiO2 (n = 4, 7) *ACS Catal.* **2020**, *10*, 4543-4558.
28. Yang, F.; Wang, Y.; Cui, Y.; Yang, X.; Zhu, Y.; Weiss, C. M.; Li, M.; Chen, G.; Yan, Y.; Gu, M. D.; Shao, M. Sub-3 nm Pt@Ru toward Outstanding Hydrogen Oxidation Reaction Performance in Alkaline Media. *J. Am. Chem. Soc.* **2023**, *145*, 27500-27511.
29. Zhang, S.; Hao, Y.; Su, D.; Doan-Nguyen, V. V. T.; Wu, Y.; Sun, S.; Murray, C. B. Monodisperse Core/Shell Ni/FePt Nanoparticles and Their Conversion to Ni/Pt to Catalyze Oxygen Reduction. *J. Am. Chem. Soc.* **2014**, *136*, 15921-15924.
30. Alinezhad, A.; Gloag, L.; Benedetti, T. M.; Cheong, S.; Webster, R. F.; Roelsgaard, M.; Iversen, B. B.; Schuhmann, W.; Gooding, J. J.; Tilley, R. D. Direct Growth of Highly Strained Pt Islands on Branched Ni Nanoparticles for Improved Hydrogen Evolution Reaction Activity. *J. Am. Chem. Soc.* **2019**, *141*, 16202-16207.
31. Hirai, H.; Takano, S.; Nakashima, T.; Iwasa, T.; Taketsugu, T.; Tsukuda, T. Doping-Mediated Energy-Level Engineering of M@Au_{12} Superatoms (M=Pd, Pt, Rh, Ir) for Efficient Photoluminescence and Photocatalysis. *Angew. Chem., Int. Ed*. **2022**, *61*, e202207290.
32. Dhital, R. N. Kamonsatikul, C.; Somsook, E. Bobuatong, K.; Ehara, M.; Karanjit, S.; Sakurai, H. Low-Temperature Carbon–Chlorine Bond Activation by Bimetallic Gold/Palladium Alloy Nanoclusters: An Application to Ullmann Coupling. *J. Am. Chem. Soc.* **2012**, *134*, 20250-20253.
33. Miura, H.; Tanaka, Y.; Nakahara, K.; Hachiya, Y.; Endo, K.; Shishido, T. Concerted Catalysis by Adjacent Palladium and Gold in Alloy Nanoparticles for the Versatile and Practical [2+2+2] Cycloaddition of Alkynes. *Angew. Chem., Int. Ed*. **2018**, *57*, 6136-6140.
34. Min, H.; Miyamura, H.; Yasukawa, T.; Kobayashi, S. Heterogeneous Rh and Rh/Ag bimetallic nanoparticle catalysts immobilized on chiral polymers. *Chem. Sci.* **2019**, *10*, 7619-7626.
35. Tian, K.; Liu, W.-J.; Zhang, S.; Jiang, H. One-Pot Synthesis of a Carbon Supported Bimetallic Cu-Ag NPs Catalyst for Robust Catalytic Hydroxylation of Benzene to Phenol by Fast Pyrolysis of Biomass Waste. *Green Chem.* **2016**, *18*, 5643–5650.
36. Verma, S.; Nasir Baig, R. B.; Nadagouda, M. N.; Varma, R. S. Hydroxylation of Benzene via C–H Activation using Bimetallic CuAg@g-C_3N_4. *ACS Sustainable Chem. Eng.* **2017**, *5*, 3637–3640.
37. Saha, R.; Arunprasath, D.; Sekar, G. Surface Enriched Palladium on Palladium-Copper Bimetallic Nanoparticles as Catalyst for Polycyclic Triazoles Synthesis. *J. Catal*. **2019**, *377*, 673–683.
38. Huang, F.; Wang, F.; Hu, Q.; Tang, L.; Xu, D.; Fang, Y.; Zhang, W. Monodisperse CuPd Alloy Nanoparticles as Efficient and Reusable Catalyst for the C(sp^2)–H Bond Activation. *Appl. Organomet. Chem*. **2021**, *35*, e6236.
39. Hasegawa, S.; Harano, K.; Motokura, K. RhRu Bimetallic Oxide Cluster Catalysts for Cross-Dehydrogenative Coupling of Arenes and Carboxylic Acids. *J. Am. Chem. Soc*. **2024**, *146*, 19059–19069.
40. Li, C.; Sato, R.; Kanehara, M.; Zeng, H.; Bando, Y.; Teranishi, T. Controllable Polyol Synthesis of Uniform Palladium Icosahedra: Effect of Twinned Structure on Deformation of Crystalline Lattices. *Angew. Chem., Int. Ed.* **2009**, *48*, 6883–6887.
41. Zhao, J.; Wang, M.; Peng, Y.; Ni, J.; Hu, S.; Zeng, J.; Chen, Q. Exploring the Strain Effect in Single Particle Electrochemistry using Pd Nanocrystals. *Angew. Chem., Int. Ed.* **2023**, *135*, e202304424.
42. Xiong, Y.; Chen, J.; Wiley, B.; Xia, Y.; Aloni, S.; Yin, Y. Understanding the Role of Oxidative Etching in the Polyol Synthesis of Pd Nanoparticles with Uniform Shape and Size. *J. Am. Chem. Soc.* **2005**, *127*, 7332–7333.
43. Zhang, H.; Jin, M.; Xiong, Y.; Lim, B.; Xia, Y. Shape-Controlled Synthesis of Pd Nanocrystals and Their Catalytic Applications. *Acc. Chem. Res.* **2013**, *46*, 1783–1794.
44. García-Cuadrado, D.; de Mendoza, P.; Braga, A. A. C.; Maseras, F.; Echavarren, A. M. Proton-Abstraction Mechanism in the Palladium-Catalyzed Intramolecular Arylation: Substituent Effects. *J. Am. Chem. Soc.* **2007**, *129*, 6880–6886.

45. Lapointe, D.; Fagnou, K. Overview of the Mechanistic Work on the Concerted Metallation-Deprotonation Pathway. *Chem. Lett*. **2010**, *39*, 1118–1126.
46. Ackermann, L. Carboxylate-Assisted Transition-Metal-Catalyzed C–H Bond Functionalizations: Mechanism and Scope. *Chem. Rev.* **2011**, *111*, 1315–1345.
47. Gorelsky, S. I.; Lapointe, D.; Fagnou, K. Analysis of the Palladium-Catalyzed (Aromatic)C–H Bond Metalation–Deprotonation Mechanism Spanning the Entire Spectrum of Arenes. *J. Org. Chem.* **2012**, *77*, 658–668.
48. Davies, D. L.; Macgregor, S. A.; McMullin, C. L. Computational Studies of Carboxylate-Assisted C–H Activation and Functionalization at Group 8–10 Transition Metal Centers. *Chem. Rev*. **2017**, *117*, 8649–8709.
49. Frisch, M. J.; Trucks, G. W.; Schlegel, H. B.; Scuseria, G. E.; Robb, M. A.; Cheeseman, J. R.; Scalmani, G.; Barone, V.; Petersson, G. A.; Nakatsuji, H.; Li, X.; Caricato, M.; Marenich, A. V.; Bloino, J.; Janesko, B. G.; Gomperts, R.; Mennucci, B.; Hratchian, H. P.; Ortiz, J. V.; Izmaylov, A. F.; Sonnenberg, J. L.; Williams; ; Ding, F.; Lipparini, F.; Egidi, F.; Goings, J.; Peng, B.; Petrone, A.; Henderson, T.; Ranasinghe, D.; Zakrzewski, V. G.; Gao, J.; Rega, N.; Zheng, G.; Liang, W.; Hada, M.; Ehara, M.; Toyota, K.; Fukuda, R.; Hasegawa, J.; Ishida, M.; Nakajima, T.; Honda, Y.; Kitao, O.; Nakai, H.; Vreven, T.; Throssell, K.; Montgomery, J. A., Jr.; Peralta, J. E.; Ogliaro, F.; Bearpark, M. J.; Heyd, J. J.; Brothers, E. N.; Kudin, K. N.; Staroverov, V. N.; Keith, T. A.; Kobayashi, R.; Normand, J.; Raghavachari, K.; Rendell, A. P.; Burant, J. C.; Iyengar, S. S.; Tomasi, J.; Cossi, M.; Millam, J. M.; Klene, M.; Adamo, C.; Cammi, R.; Ochterski, J. W.; Martin, R. L.; Morokuma, K.; Farkas, O.; Foresman, J. B.; Fox, D. J. Gaussian 16 Rev. C.01; Gaussian, Inc.: Wallingford, CT, 2016.
50. Perdew, J. P.; Burke, K.; Ernzerhof, M. Generalized Gradient Approximation Made Simple. *Phys. Rev. Lett.* **1996**, *77*, 3865–3868.
51. Grimme, S.; Antony, J.; Ehrlich, S.; Krieg, H. A consistent and accurate ab initio parameterization of density functional dispersion correction (DFT-D) for the 94 elements H–Pu. *J. Chem. Phys.* **2010**, *132*, 154104.
52. Nava, P.; Sierka, M.; Ahlrichs, R. Density Functional Study of Palladium Clusters. *Phys. Chem. Chem. Phys.* **2003**, *5*, 3372–3381.
53. Chaves, A. S.; Piotrowski, M. J.; Da Silva, J. L. F. Evolution of the Structural, Energetic, and Electronic Properties of the 3d, 4d, and 5d Transition-Metal Clusters (30 TMn Systems for n = 2–15): A Density Functional Theory Investigation. *Phys. Chem. Chem. Phys.* **2017**, *19*, 15484–15502.
54. Wang, L.; Carrow, B. P. Oligothiophene Synthesis by a General C–H Activation Mechanism: Electrophilic Concerted Metalation-Deprotonation (eCMD). *ACS Catal*. **2019**, *9*, 6821–6836.
55. Evans, R.; Sampson, J.; Wang, L.; Lückemeier, L.; Carrow, B. P. Ligand Switchable Site Selectivity in C–H Alkenylation of Thiophenes by Turnover-Limiting Step Control. *Chem. Commun*. **2021**, *57*, 9076–9079.
56. Piszel, P. E.; Orzolek, B. J.; Olszewski, A. K.; Rotella, M. E.; Spiewak, A. M.; Kozlowski, M. C.; Weix, D. J. Protodemetalation of (Bipyridyl)Ni(II)–Aryl Complexes Shows Evidence for Five-, Six-, and Seven-Membered Cyclic Pathways. *J. Am. Chem. Soc.* **2023**, *145*, 8517–8528.

TOC graphic: